

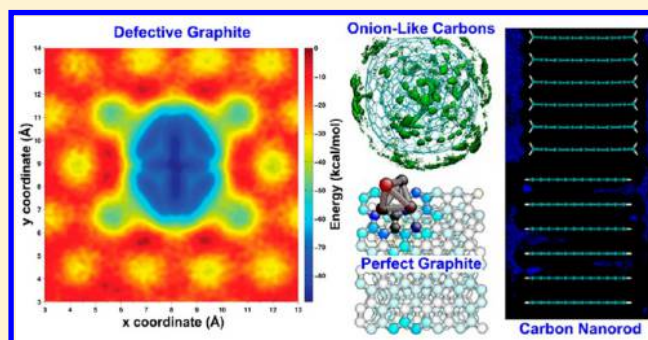
# Reactive Force Field Study of Li/C Systems for Electrical Energy Storage

Muralikrishna Raju,<sup>†</sup> P. Ganesh,<sup>\*,§</sup> Paul R. C. Kent,<sup>§,||</sup> and Adri C. T. van Duin<sup>\*,‡</sup>

<sup>†</sup>Department of Physics and <sup>‡</sup>Department of Mechanical and Nuclear Engineering, The Pennsylvania State University, University Park, Pennsylvania 16802, United States

<sup>§</sup>Center for Nanophase Materials Sciences and <sup>||</sup>Computer Science and Mathematics Division, Oak Ridge National Laboratory, Oak Ridge, Tennessee 37831, United States

**ABSTRACT:** Graphitic carbon is still the most ubiquitously used anode material in Li-ion batteries. In spite of its ubiquity, there are few theoretical studies that fully capture the energetics and kinetics of Li in graphite and related nanostructures at experimentally relevant length, time-scales, and Li-ion concentrations. In this paper, we describe the development and application of a ReaxFF reactive force field to describe Li interactions in perfect and defective carbon-based materials using atomistic simulations. We develop force field parameters for Li–C systems using van der Waals-corrected density functional theory (DFT). Grand canonical Monte Carlo simulations of Li intercalation in perfect graphite with this new force field not only give a voltage profile in good agreement with known experimental and DFT results but also capture the in-plane Li ordering and interlayer separations for stage I and II compounds. In defective graphite, the ratio of Li/C (i.e., the capacitance increases and voltage shifts) both in proportion to the concentration of vacancy defects and metallic lithium is observed to explain the lithium plating seen in recent experiments. We also demonstrate the robustness of the force field by simulating model carbon nanostructures (i.e., both 0D and 1D structures) that can be potentially used as battery electrode materials. Whereas a 0D defective onion-like carbon facilitates fast charging/discharging rates by surface Li adsorption, a 1D defect-free carbon nanorod requires a critical density of Li for intercalation to occur at the edges. Our force field approach opens the opportunity for studying energetics and kinetics of perfect and defective Li/C structures containing thousands of atoms as a function of intercalation. This is a key step toward modeling of realistic carbon materials for energy applications.



## I. INTRODUCTION

Graphitic carbon is the most ubiquitously used anode material in Li-ion batteries<sup>1–5</sup> (LIBs). This is due to its low cost, low voltage with respect to lithium allowing for higher cell voltages when paired with oxide cathodes, reasonable capacity, and modest volume expansion upon lithiation. However, the achievable rates in graphite, determined by the diffusion of lithium, are lower than desired ( $D_{\text{Li}} \sim 10^{-6} \text{ cm}^2 \text{ s}^{-1}$ ).<sup>6</sup> Lithium insertion into graphite further produces ordered solid phases that lead to significant strain, latent heat-induced losses, and mechanical damage during cycling.<sup>7–9</sup> Ideally, one would like to improve capacity and rates without any loss in cyclability, leading to a longer lifetime. Most of the simulations on Li-graphite systems to date have focused on defect-free graphite with no rigorous treatment of vacancies, even though experiments show that defective graphite can indeed allow increased rates.<sup>10</sup> Recent theoretical studies in graphene and graphite indicate that defects, vacancies, and curvature strongly affect lithium adsorption energies.<sup>11,12</sup> Defective graphene also enhances reduction of oxygen, a key step in Li–air batteries.<sup>13</sup> This suggests urgency in improving our microscopic understanding of the Li intercalation process in graphitic systems and

a need to explore the degree of variability in the voltage, rates, capacity, and cyclability of defective graphite.

The challenge in modeling Li intercalations comes from the coupling between weakly van der Waals-bonded graphite and charge-transfer of lithium metal atoms to graphite.<sup>14</sup> This coupling, combined with the electrostatic interaction of the ions in the solid, gives rise to many different types of ordered solid phases. Density functional theory (DFT) calculations with van der Waals corrections are able to predict theoretical voltage curves and diffusion barriers for a single lithium ion in experimentally known solid phases<sup>6</sup> and in nanotubes.<sup>15,16</sup> However, DFT rapidly becomes prohibitively computationally costly<sup>17</sup> at the large system sizes and time scales needed to study defective materials, nanoscale materials, phase transitions, lithium intercalation, and charge–discharge dynamics at realistic concentrations. Force field methods are required to study this regime. Because of the charge-transfer nature of this system, a reactive force field is required to study this phenomenon.

Received: November 18, 2014

Published: April 2, 2015



In this paper, we fit a reactive force field for the Li/C system using the ReaxFF formalism and study the microscopic features of lithium intercalation/deintercalation using a grand canonical Monte Carlo simulation involving approximately a thousand atoms in a variety of carbon structures. We differentiate atomistic processes that occur in single-layer graphene and bulk graphite with those occurring on surfaces and edges and capture the staging effect seen in graphite.<sup>5,18</sup> We study graphite with realistic concentrations of both point and topological defects (1–2% defect density) and determine quantitatively how the staging effects are changed. Finally, we perform simulations for two carbon nanostructures: a 0D carbon-onion and a 1D carbon nanorod. The novel insights we gain about Li intercalation in these carbon nanostructures with and without defects demonstrates the utility of reactive force fields in gaining a microscopic understanding of processes in energy materials by atomistic simulations of thousands of atoms in a reactive environment.

## II. COMPUTATIONAL METHODS

**A. ReaxFF Reactive Method.** A detailed description of the ReaxFF is given in van Duin et al.<sup>19</sup> and Chenoweth et al.<sup>20</sup> In the ReaxFF reactive force field, the total (system) energy is given by

$$E_{\text{system}} = E_{\text{bond}} + E_{\text{val}} + E_{\text{tors}} + E_{\text{over}} + E_{\text{under}} + E_{\text{lp}} + E_{\text{vdwaals}} + E_{\text{coulomb}} \quad (1)$$

The terms in eq 1 include bond energies ( $E_{\text{bond}}$ ), valence-angle energies ( $E_{\text{val}}$ ), torsion-angle energies ( $E_{\text{tors}}$ ), energy to penalize overcoordination of atoms ( $E_{\text{over}}$ ), energy to stabilize undercoordination of atoms ( $E_{\text{under}}$ ), lone-pair energies ( $E_{\text{lp}}$ ), and terms to handle nonbonded van der Waals ( $E_{\text{vdwaals}}$ ) and Coulomb ( $E_{\text{coulomb}}$ ) interactions.

ReaxFF employs a bond order/bond energy relationship, which allows for bond formation and bond dissociation during molecular dynamics (MD) simulations. The bond orders are obtained from interatomic distances and are updated at every MD or energy minimization step. All connectivity dependent interactions (e.g., valence- and torsion-angle energies) are bond-order dependent, and therefore, energies and forces associated with these terms go to zero upon bond dissociation. ReaxFF calculates nonbonded interactions (van der Waals and Coulomb) between every atom pair, irrespective of their connectivity, and excessive short-range nonbonded interactions are avoided by incorporating a shielding term in these interactions.

Computationally, the ReaxFF formalism is fast enough to permit the calculation of thousands of atoms on modest computational resources. For example, the molecular dynamics simulations of onion-like carbons described later involved 6475 atoms. We were able to obtain 118 steps per minute on a 4 processing core workstation, whereas the equivalent DFT calculation would not be possible even using the largest supercomputers. Parallel molecular dynamics simulators like LAMMPS<sup>21</sup> and ADF<sup>22</sup> allow atomistic simulations of hundreds of thousands of atoms on high performance computing systems, enabling modeling of realistic carbon materials. The ReaxFF formalism has been previously employed to investigate lithiated sulfur cathode materials,<sup>23</sup> lithiated Si nanowires,<sup>24</sup> and amorphous  $\text{Li}_x\text{Si}$  alloys.<sup>25</sup>

**B. Fitting the ReaxFF Parameters for Li/C Systems.** In the current study, we develop optimized parameters for Li/C

systems. The training set of data used to fit these parameters is a collection of results (energies, geometries, charges, etc.) derived from quantum-mechanical (QM) calculations. The parameters for pure carbon were previously used in Yang et al.<sup>26</sup> and Huang et al.<sup>27</sup>

**Ab Initio Calculations.** The force field is trained against a set of density functional theory-based data sets. The long ranged van der Waals interactions between carbon atoms are captured via the Grimme parametrization<sup>28</sup> using the DFT-D2 formalism as implemented in the VASP package.<sup>29,30</sup> All calculations use the PBE functional and a converged k-point mesh corresponding to one point per  $0.0008 \text{ \AA}^{-3}$ . Lithium polarizability is set to zero (i.e.,  $C_6^{\text{Li}} = 0$ ) as was shown to be necessary to capture lithium diffusion barriers in graphite as well as the structural parameters of fully lithiated graphite,  $\text{LiC}_6$ .<sup>14,31</sup> The following data are used to train the force field: (1) cohesive energy and elastic constants of AA, AB, rhombohedral graphite, and  $\text{LiC}_6$ , (2) the lithium diffusion barriers in AA graphite at interplanar spacings of 3.35, 3.52, and 3.706 Å, (3) lithium adsorption energies on perfect and single vacancy defect graphene, and (4) the different types of lithium clusters on graphene and defective graphene (different reconstructions of vacancies and divacancies). This data is chosen to be representative of the geometries and electronic configurations likely to be found in pure and defective graphite for varying local lithium concentrations while remaining small enough to be suitable for training.

On pristine graphene, two Li atoms form a dimer with  $d(\text{Li-Li}) = 2.91 \text{ \AA}$  with one of the Li atoms on the hollow hexagonal site 1.91 Å above the graphene plane. Three Li atoms form a coplanar, isosceles triangle of side 2.86 Å perpendicular to the graphene plane with two of the atoms on the hollow site at a height of 1.93 Å. Four Li atoms form a prismatic cluster with three coplanar atoms at the hollow site of graphene at a height of 1.86 Å. For a single atom vacancy defect, Li atoms bind to the underbonded  $\text{sp}^3\text{-C}$  atom with a bond distance of  $d(\text{Li-C}) \sim 2\text{--}2.08 \text{ \AA}$  with up to 2 Li atoms per underbonded  $\text{sp}^3\text{-C}$ . Cluster formation begins at three Li atoms, similar to the case of pristine graphene, with four atoms forming an interesting inverted prismatic cluster at the center of the defect with a  $d(\text{Li-Li}) \sim 1.98 \text{ \AA}$ . For a 5–8–5 reconstructed graphene due to a divacancy, single lithium is at a height of 1.43 Å at the center of the octagon with very little puckering of the graphene layer. The presence of two Li atoms leads to strong puckering when one of the Li atoms forms bonds with the atoms around the defect and a  $d(\text{Li-Li}) = 2.33 \text{ \AA}$ . The bonded Li atom substitutes for the two missing carbon atoms, giving rise to puckering due to a nonzero curvature effect. However, this type of Li atom arrangement is higher in energy by 0.6 eV than a coplanar arrangement with one Li at the center of the octahedral site and another at the pentagonal site with  $d(\text{Li-Li}) = 2.964 \text{ \AA}$  with no puckering of graphene. This suggests that the Li–C interaction dominates over metallic interactions between Li atoms, possibly due to local charge transfer processes. However, with an extra Li atom, formation of a three-dimensional cluster through the defect is more stable than an arrangement with adsorbed geometries of individual Li atoms. With four atoms, Li atoms form a trigonal pyramidal Li cluster with one atom at the center of the octahedral site, suggesting a strong tendency to form metal clusters instead of ion adsorption on graphene. For a 5–5–5–7–7–7 reconstruction of the graphene defect, a single Li atom sits on the C atom at the intersection of the 7–7–7 rings at a distance of 2.04 Å. Interestingly, two Li atoms form a dimer above this C

atom with  $d(\text{Li-Li}) = 3.10 \text{ \AA}$ . Three Li atoms form an isosceles triangular geometry with the other two atoms on top of the pentagonal sites.

The Li-H parameters were trained against DFT data for the Li-H bond dissociation in the LiH molecule and for the LiH (fcc) equation of state. The force field obtains a LiH equilibrium bond distance of  $1.55 \text{ \AA}$  (DFT distance =  $1.62 \text{ \AA}$ ) and dissociation energy of  $2.05 \text{ eV}$  (DFT dissociation energy =  $2.53 \text{ eV}$ ). For the LiH (fcc) crystal, the force field obtains an equilibrium density of  $0.713 \text{ kg/dm}^3$  (DFT density =  $0.89 \text{ kg/dm}^3$ ). These Li/H DFT data were given relatively low weights in the training, and the Li/H parameters were trained against Li---H nonbonded interactions in Li/hydrocarbon clusters.

A recent study by Ganesh et al.<sup>14</sup> compares van der Waals-included DFT calculations of adsorption and diffusion of atomic lithium in AA-stacked graphite with highly accurate diffusion quantum Monte Carlo (QMC) studies. The study observes: (i) DFT-D2 slightly overestimates the binding energy of AA-stacked graphite, especially at smaller lattice constants (e.g., by  $12 \text{ meV}$  at  $3.36 \text{ \AA}$  lattice spacing) and (ii) DFT-D2 overestimates the diffusion barriers of Li in AA-stacked graphite, especially at larger separations of the graphite planes (e.g., by  $0.3 \text{ eV}$  at  $3.7 \text{ \AA}$  lattice spacing).

**Force Field Optimization.** To optimize the bond parameters for Li-C, we utilized a successive one-parameter search technique to minimize the sum-of-squares error function

$$\text{Error} = \sum_i^n \left[ \frac{(\chi_{i,\text{QM}} - \chi_{i,\text{ReaxFF}})^2}{\sigma_i} \right] \quad (2)$$

where  $\chi_{i,\text{QM}}$  is a QM value,  $\chi_{i,\text{ReaxFF}}$  is a ReaxFF calculated value, and  $\sigma_i$  is the weight assigned to data point  $i$ . We fit a total of 10 parameters (Table 1) to a training set containing 389 data

**Table 1. Fitted Parameters Optimized in this Li-C Force Field Development Study**

bond parameters (Li-C parameters)					
sigma-bond dissociation energy (edis1)	bond energy (pbe1)	bond energy (pbe2)	$\pi$ bond order (pbo3)	$\sigma$ bond order (pbo1)	$\sigma$ bond order (pbo2)
82.8122	0.9497	0.1520	-0.2500	-0.1991	5.1849
off diagonal parameters (Li-C parameters)					
Ediss	Rvdw	Alfa	Cov.r		
0.2964	1.9000	10.8828	1.5947		

points using a successive single-parameter search method and multiple cycles to account for parameter correlation. The fitted Li/C parameters are presented in Table 1.

**Force Field Validation.** In this section, we compare ReaxFF with the training set DFT data corresponding to structures and energies of Li adsorption and diffusion in graphene and graphite.

We consider three sites with high symmetry to analyze the adsorption of Li on graphene: the site in the center of a hexagon (Hollow), the site at the midpoint of a carbon-carbon bond (Bridge), and the site on top of a carbon atom (Top). Table 2 gives the comparison of ReaxFF and DFT values for Li adsorption on graphene at these sites. The adsorption energy  $E_{\text{ad}}$  is defined as

$$E_{\text{ad}} = E_{\text{Li+g}} - E_{\text{g}} - nE_{\text{Li}} \quad (3)$$

**Table 2. Comparison of ReaxFF and DFT Values for Various Adsorption Energies of Li in Graphene and Graphite**

	ReaxFF (kcal/mol)	DFT (kcal/mol)
Li adsorption energy (AE) on Hollow site in graphene	12.63	12.08
Li AE on Bridge site in graphene	19.70	19.08
Li AE on Top site in graphene	22.0	21.48
Li in graphite (formation energy of $\text{LiC}_6$ )	-2.74	-2.76

where  $E_{\text{Li+g}}$  is the energy of graphene with Li adsorbed on it,  $E_{\text{Li}}$  is the energy of one metallic (body-centered cubic) Li atom,  $E_{\text{g}}$  is the energy of isolated graphene, and  $n$  is the number of adsorbed Li atoms. The Li reference state is the stable bulk phase (bcc-lithium); thus, the adsorption energy measures the stability of Li-adsorbed single layer graphene (SLG) against pristine SLG and metallic Li. The geometry structure and energies are obtained after the positions of all atoms have been relaxed.

The force field is also parametrized against the dissociation pathways of the C-Li bond in  $\text{CH}_3\text{-Li}$  and  $\text{C}_6\text{H}_5\text{-Li}$ . The ReaxFF values for bond dissociation energy and equilibrium bond length of the C-Li bond in  $\text{CH}_3\text{-Li}$  ( $2.31 \text{ eV}$ ,  $1.96 \text{ \AA}$ ) and  $\text{C}_6\text{H}_5\text{-Li}$  ( $2.33 \text{ eV}$ ,  $1.97 \text{ \AA}$ ) are in good agreement with the DFT values of ( $2.39 \text{ eV}$ ,  $1.91 \text{ \AA}$ ) and ( $2.60 \text{ eV}$ ,  $1.97 \text{ \AA}$ ), respectively. We observe that ReaxFF reproduces the equilibrium distance and overall bond strength accurately, but that the bond dissociates more quickly in the ReaxFF description compared to the DFT results. This set of nonperiodic DFT calculations are performed using the B3LYP functional as implemented in the Gaussian package.<sup>32</sup>

To further validate the force field, we investigated Li intercalation and diffusion in pure graphite. When multiple graphene sheets are stacked to form graphite, the only binding forces between adjacent layers are weak van der Waals (vdW) interactions. As Li is intercalated, the C-C vdW bonds are perturbed and screened by hybridization between the Li ions and carbon atoms. This is evidenced in the change from AB hexagonal stacking (graphite) to AA stacking in stage I compounds.<sup>5,18</sup> As shown in Table 2, ReaxFF gives formation energy of stage I ( $\text{LiC}_6$ ) compounds that is in good agreement with DFT calculations, indicating that ReaxFF accurately captures the hybridization. To investigate Li diffusion, we considered separations between graphene layers of  $3.35$  and  $3.7 \text{ \AA}$  in AA graphite. Figure 1 shows a comparison of potential energy curves of Li diffusion along two symmetrical paths: Hollow-Bridge-Hollow, and Hollow-Top-Bridge-Top-Hollow. ReaxFF shows very good agreement with DFT calculations for the studied diffusion paths: for the first path, the transition state energies are  $27.20$  and  $12.70 \text{ kcal/mol}$ , whereas for the second path, the transition energies are  $32.87$  and  $15.33 \text{ kcal/mol}$  at separations of  $3.35$  and  $3.7 \text{ \AA}$ , respectively.

### III. RESULTS AND DISCUSSION

Comparisons with DFT and experimental results in this section provide out of training-set validation for the force field.

**A. Adsorption and Diffusion of Lithium on Defective Graphene.** Lithium motion on pristine graphene is restricted to two-dimensional diffusion. Lithium diffusion in the direction perpendicular to the graphene sheet is extremely energetically unfavorable. The diffusion barrier for Li in the direction



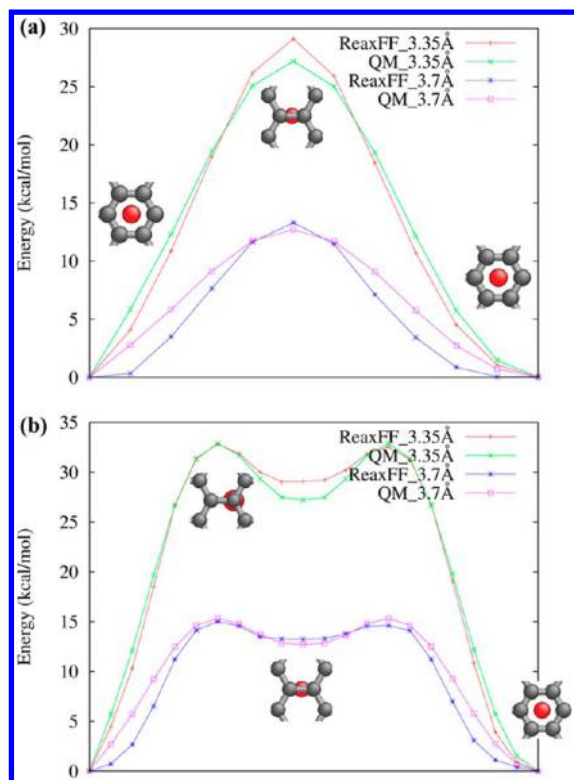


**Figure 1.** Comparison of potential energy curves of Li diffusion along the (a) Hollow–Bridge–Hollow and (b) Hollow–Top–Bridge–Top–Hollow paths in graphite at separations of 3.35 and 3.7 Å as predicted by ReaxFF and DFT calculations.

perpendicular to pristine graphene given by ReaxFF (8.87 eV) is in good agreement with DFT (8.74 eV).<sup>33</sup> Intuitively, defects

in graphene can reduce the diffusion barrier of lithium. We investigated the diffusion of Li in the direction perpendicular to the graphene sheet for two cases: graphene with single and divacancy. Figure 2 shows the energy landscape for lithium diffusion in the direction perpendicular to the graphene sheet for graphene with single and divacancy. The ReaxFF values for the local minimum, diffusion barrier, and position of local minimum for the two cases are in good agreement with the corresponding DFT values,<sup>33</sup> suggesting the general applicability of our force field method to defective carbonaceous materials.

**B. Li Intercalation in Pristine and Defective Graphite–Voltage Profiles.** We apply hybrid grand canonical Monte Carlo/molecular dynamics (GCMC/MD) simulations<sup>34,35</sup> based on the Metropolis algorithm to obtain a set of ground states consistent with first-principles data. The possible MC moves include: (1) inserting a lithium atom into the system at a random position, (2) removing a randomly selected lithium atom from the system, and (3) moving a lithium atom to a new random position in the system. Coordinates for Li insertion and Li move steps were chosen randomly such that any unoccupied position in the simulation box could be selected. In our hybrid method, we introduce an energy minimization step after each MC trial move. In this study, the energy minimization step consists of a conjugate gradient (CG) geometry optimization with a convergence criterion of 0.5 kcal/mol between subsequent CG steps. This step is necessary to allow the expansion of graphite on Li intercalation. The GCMC temperature scans at constant chemical potential are combined with molecular dynamics runs of 12.5 ps in the NVT ensemble for every 50 successful GCMC moves. The hybrid GCMC/MD method allows the movement of C and intercalated Li atoms during the energy minimization and MD runs and enables the system to explore phase space at the simulation temperature.

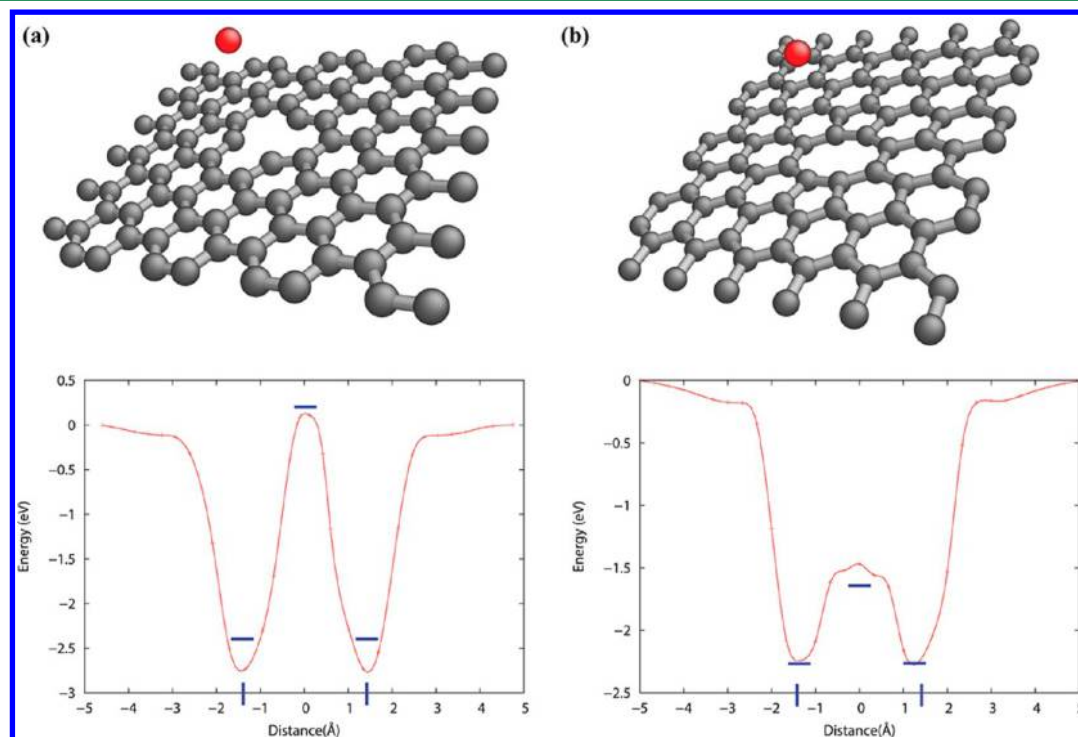


**Figure 2.** Potential energy curves for lithium diffusion in the direction perpendicular to the graphene sheet for graphene with (a) monovacancy and (b) divacancy. The blue dashes are DFT values for the local minimum, diffusion barrier, and position of local minimum.

This enables the method to investigate the role of intercalated Li on subsequent intercalation. The development and implementation of the hybrid GCMC/MD method in Reax is described in detail in Senffle et al.<sup>34,35</sup>

**Bulk Graphite.** To explore Li loading in bulk graphite, we used a periodic ( $6 \times 6 \times 8$ ) supercell, corresponding to 8 graphene layers. GCMC simulations are performed at a constant external chemical potential of Li at a temperature of 300 K until maximum Li loading. The external chemical potential of Li was fixed at the total energy of a single lithium atom in body-centered cubic lithium. Figure 3(a) shows the in-

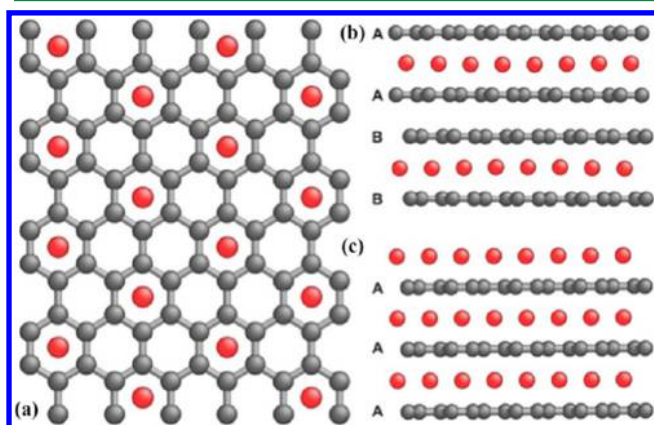


**Figure 3.** (a) In-plane Li ordering in stage I and II compounds as seen from above on the carbon honeycomb lattice. (b) Li–C stacking in stage II and (c) stage I.

plane Li ordering (checkerboard pattern) for stage I and II compounds predicted by ReaxFF in agreement with previous DFT calculations.<sup>5</sup> ReaxFF also reproduces the Li–C stacking sequence in stage I and II compounds as shown in Figure 3(b).

The average potential as a function of Li intercalation content in a material is calculated as

$$V(x) = -\frac{G(\text{Li}_{x+\Delta x}\text{C}_6) - G(\text{Li}_x\text{C}_6) - \Delta x G(\text{Li})}{\Delta x} \quad (4)$$

where  $G$  is the Gibbs free energy of the compound. Because the term  $P\Delta V$  is on the order of  $10^{-5}$  eV,<sup>36</sup> and the term  $T\Delta S$  is on the order of the thermal energy (26 meV at 300 K), the pressure and entropy terms can be neglected, and the Gibbs free energy can be replaced with ground-state energies with little error.<sup>5,36,37</sup> Figure 4(a) shows the voltage profile in  $\text{Li}_x\text{C}_6$  obtained using ReaxFF as a function of  $x$  in  $\text{Li}_x\text{C}_6$ , which is in good agreement with the experimental voltage profile.<sup>38</sup> The voltage profile reflects the sequence of phase transitions in the system, because the coexistence of two stable phases gives rise to plateaus. The three regions of two-phase coexistence in lithium-intercalated graphite correspond to voltage plateaus at regions of A, B, and C as shown in Figure 4(a). The first lithiated phase to become thermodynamically stable is a stage III + dilute stage II compound at  $0.12 < x < 0.25$ , followed by a dilute stage II + stage II compound at  $0.25 < x < 0.5$ , and a stage I + stage II two-phase region starting at  $x = 0.5$ . The Li concentration at the phase transitions and the phase sequence with increasing Li concentration predicted by ReaxFF is in good agreement with the experimental study by Takami et al.<sup>38</sup> Takami et al.<sup>38</sup> observed voltage plateaus at  $0.04 < x < 0.15$ ,  $0.2 < x < 0.5$ , and  $0.5 < x < 1$  during Li intercalation in graphite. ReaxFF over predicts the Li concentration at the phase

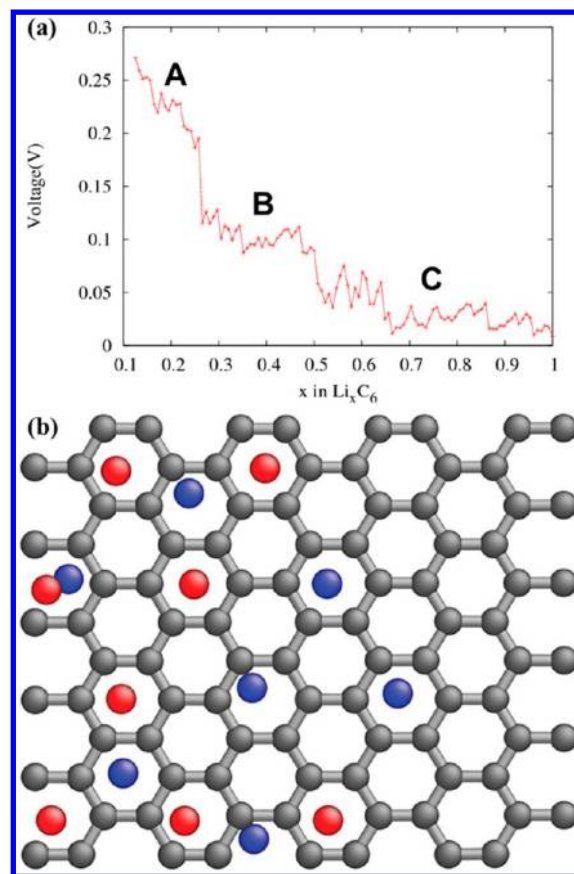


**Figure 4.** (a) Voltage profile for the Li–graphite system obtained by ReaxFF. (b) Clustering of Li up–down pairs in graphite during loading (red is up and blue is down with respect to the graphene sheet).

transition from region A to region B ( $0.25$ ) in comparison with the experimental data, which observed a gradual voltage drop over  $0.15 < x < 0.20$ .<sup>38</sup>

Experimentally, it has been deduced that Li screens the C–C van der Waals interactions.<sup>38,39</sup> Thus, there is a competition between the attractive C–C van der Waals interactions that prefers to keep the planes free of Li, the attractive Li–C interactions that promote Li intercalation, and Li–Li repulsions, which prefer to put Li ions as far apart as possible. This delicate interplay between the three interactions results in a critical Li concentration for which there is enough driving force to open and start populating an empty graphite layer to give rise to plateaus in the voltage profile. The layer spacing increased continuously with Li concentration corresponding to decreases in the voltage profile. The average spacing between graphite layers for a fully lithiated stage II compound is  $3.7 \text{ \AA}$  and stage I compound is  $3.9 \text{ \AA}$ , which is in decent agreement with experimental values of  $3.55$  and  $3.7 \text{ \AA}$ , respectively. In the stage II + stage I two-phase region, Li starts intercalating in adjacent graphite layers, and we observe clustering of up–down Li pairs as show in Figure 4(b). As Li concentration in adjacent graphite planes increases, they start sliding from AB stacking in stage II to AA stacking in stage I.

**Graphite with Single and Divacancy.** To explore Li loading in graphite with single and divacancy, we used a periodic ( $6 \times 6 \times 8$ ) supercell with single and divacancy, respectively, in one of the 8 graphene layers. This corresponds to a defect density of  $1.05\%$  for the single vacancy and  $2.01\%$  for the divacancy cases

in the defect-containing graphene layer. GCMC simulations were performed at a constant external chemical potential of Li at a temperature of 300 K until maximum stage II loading. The adsorption energy of Li on single and divacancy is larger than the adsorption energy of Li on a hollow site in graphite. This increases the voltage for Li intercalation in defective graphite, and the increase in voltage is proportional to the size of the defect as shown in Figure 5. DFT calculations of Li adsorption

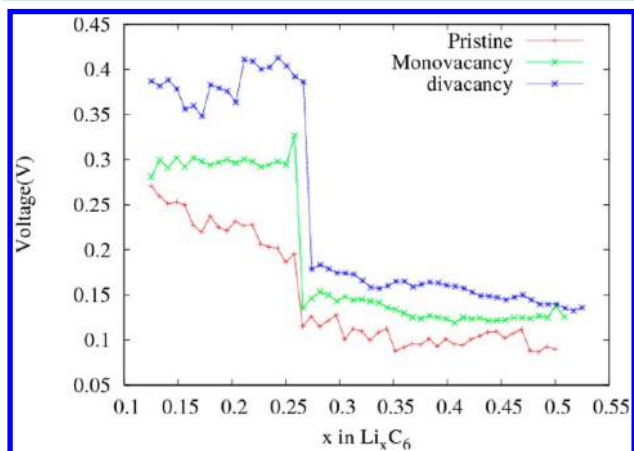


**Figure 5.** Voltage profile for Li intercalation in graphite with single and divacancy.

on defective graphene by Datta et al.<sup>37</sup> report an upward shift in lithiation potential with an increase in defect density. The enhanced adsorption energy also increases the Li/C ratio. The enhanced Li storage is, however, at the expense of an upward shift in the voltage profile. The presence of defects disturbs the in-plane ordering (checkerboard pattern) in stage I and II

compounds (see Figure 3a) as shown in Figure 6. We observe the formation of metallic Li bonds. For graphite with single vacancy, the checkerboard pattern is retained away from the vacancy, whereas in the presence of divacancy, the checkerboard pattern is lost up to the second neighboring ring from the defect.

**C. Lithium Plating.** The recent study by Rahul et al.<sup>40</sup> reports the plating of lithium metal within the interior of porous graphene networks, resulting in very high specific capacities in excess of 850 mAh g<sup>-1</sup>. DFT calculations from the same study show that the presence of 25% divacancy defects induces the formation of Li<sub>3</sub>C<sub>8</sub> in the graphene lattice, which could act as seed points for subsequent plating of lithium metal.

Using a well-tempered metadynamics simulation, we obtain the free energy surface (FES) of Li on pristine graphite and graphite with a divacancy site, as shown in Figure 7. Metadynamics is performed using version 1.3 of PLUMED<sup>41</sup> (called using a “fix” routine from LAMMPS<sup>21</sup>). The collective variables are the *x* and *y* coordinates of Li over the graphite *xy* plane. We use a hill height of 0.5 kcal/mol and a width of 0.35 Å, and hills are added at every 100 timesteps. FESs are reconstructed from the Gaussian bias potentials added during the metadynamics trajectory.

We can see from Figure 7 that divacancy sites provide a deeper and wider “potential well” for adsorption of Li with respect to hollow sites on a pristine graphite sheet, enabling graphite sheets with divacancy sites to store more Li than pristine graphite. Even at a low defect density of 2.1%, we observe a maximum capacity of ~428 mAh g<sup>-1</sup>, which corresponds to a Li/C ratio of 0.19, an ~15% increase with respect to pristine graphite. We investigate the Li clusters formed near the divacancy site as shown in Figure 6(b) and observe that Li in these clusters is more closely packed than Li

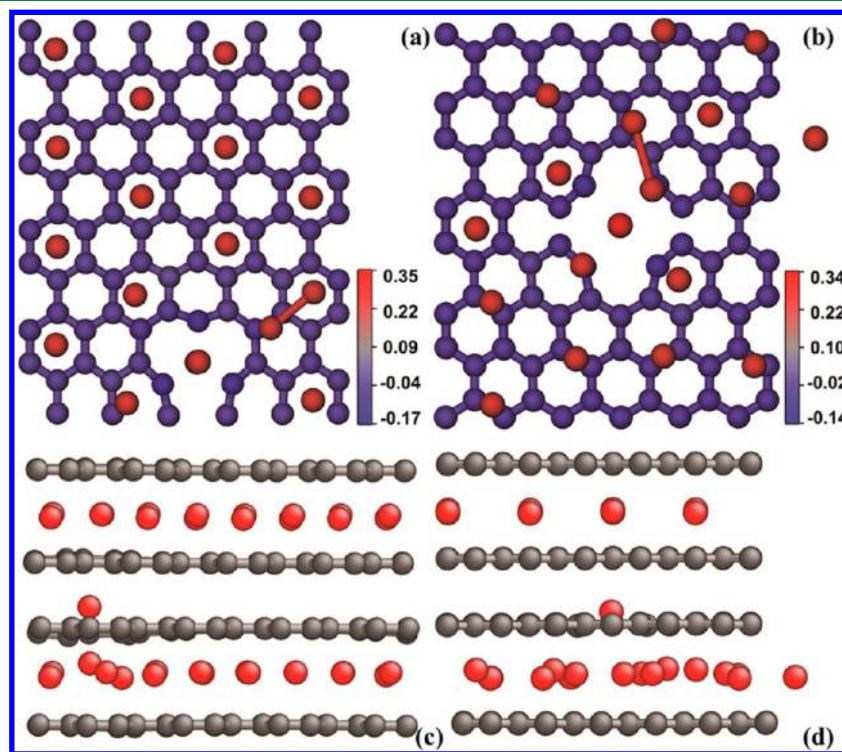


**Figure 6.** In-plane Li ordering in stage II compounds in graphite with (a) single and (b) divacancy as seen from above on the carbon honeycomb lattice. Li–C stacking in stage II compounds in graphite with (c) single and (d) divacancy.



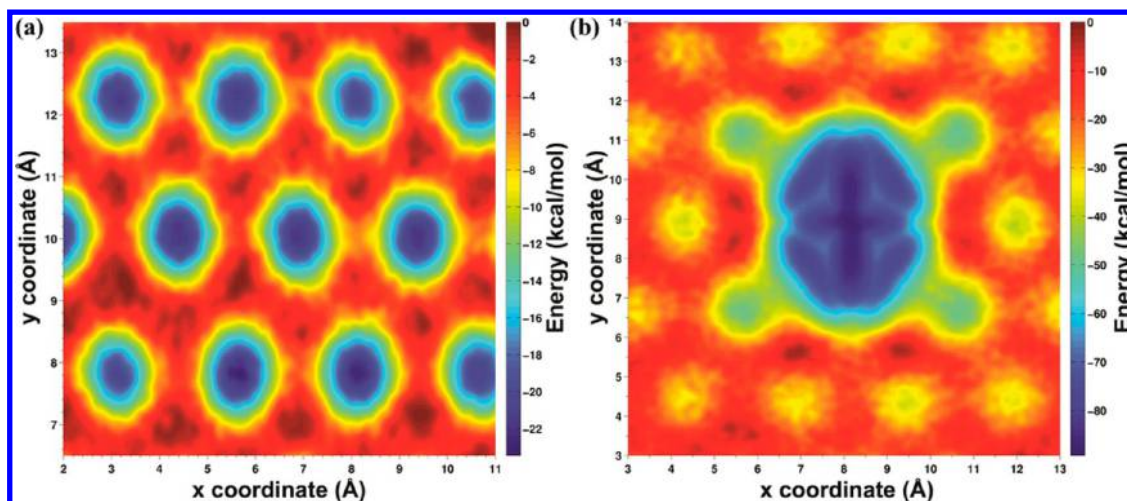


**Figure 7.** Free energy surface (FES) for adsorption of lithium on (a) pristine graphite and (b) graphite with divacancy as a function of  $x$  and  $y$  coordinates of Li with the graphite sheets placed along the  $xy$  plane.

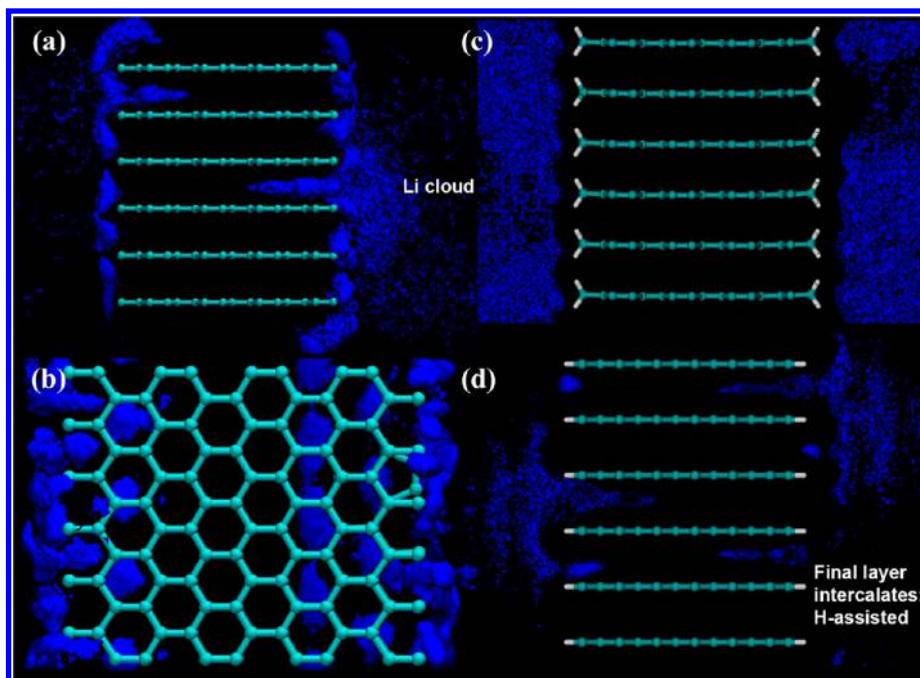


**Figure 8.** Density plot of Li (blue) during a NVT simulation at 300 K showing Li intercalation in (a) graphite: side view, (b) graphite: top view, (c) graphite with two H-terminated zigzag edges: side view and (d) graphite with H-terminated armchair edges: side view.

in  $\text{LiC}_6$  compounds in pristine graphite. The average Li–Li separation in these clusters is 3.3 Å with an average charge of +0.279e on Li, compared to an average Li–Li separation of 4.35 Å with an average charge of +0.29e on Li in stage I compounds ( $\text{LiC}_6$ ) in pristine graphite. The Li separation in these clusters is only 0.28 Å greater than Li separation of 3.03 Å in body-centered cubic lithium.<sup>42</sup> These Li also have a lower charge than  $\text{LiC}_6$  ( $t$  test,  $p < 0.001$ ). Therefore, it is reasonable to suggest that these localized high lithium content clusters could initiate subsequent plating of lithium metal at these defect sites and explain Li plating in porous graphene networks.

**D. Li Intercalation in Pristine Graphite Nanorod—Intercalation Mechanism.** Atomic-scale investigations with molecular dynamics (MD) simulations could contribute significantly to understanding Li intercalation in graphite with free edges and furnish many details of this mechanism that are

not accessible experimentally. In batteries, Li is intercalated into graphite in the presence of an electrolyte that could undergo reactions at the graphite edges to form solid–electrolyte interphases.<sup>43</sup> Here, we study intercalation at perfect edges in vacuum, thereby isolating the role of Li–Li and Li–C interactions. Lithium atoms were placed randomly on both sides of pristine graphite at least  $\sim 5$  Å away, and the systems were simulated in the canonical (NVT) ensemble at 300 K to correspond to the temperature in experimental studies. The total simulation time ranged from 500 to 750 ps, which is long enough to observe the intercalation of Li in graphite.

Li–Li repulsive intercalations are found to play a major role in facilitating Li intercalation in graphite. Li atoms at the Li–graphite interface are pushed into graphite as a result of repulsive Li–Li intercalations. The attractive Li–C interactions facilitate intercalation by opening the graphite layers. Li

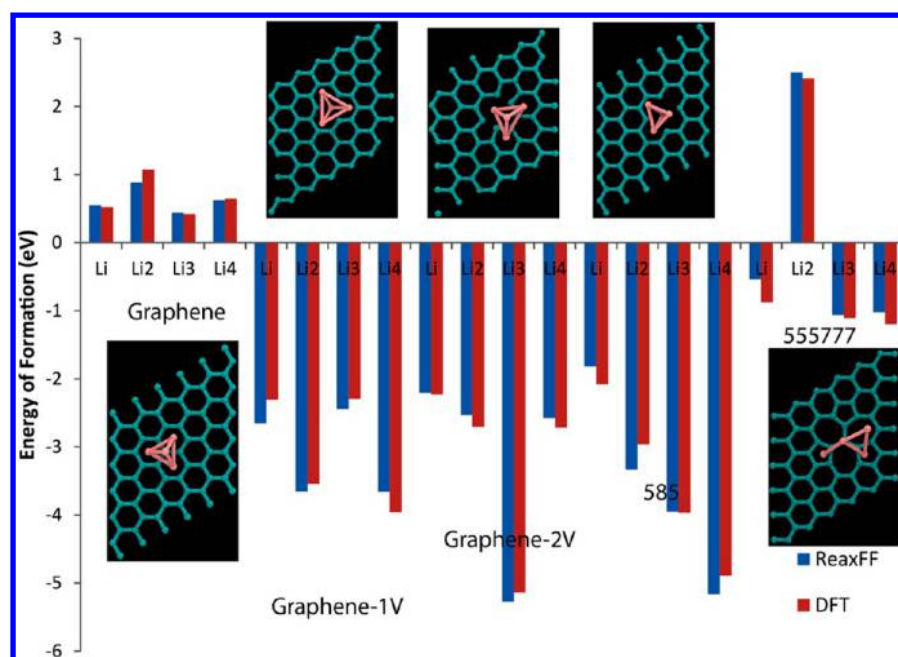


**Figure 9.** Formation energy of Li, Li-2, Li-3, and Li-4 clusters over graphene, graphene with single and divacancy, 5–8–5 reconstructed graphene, and 5–5–5–7–7–7 reconstructed graphene.

intercalation in graphite requires the presence of a cloud of Li atoms at the Li–graphite interface. In the presence of multiple Li atoms near the interface, surrounding Li atoms push the Li atoms in at the interface, and the surrounding Li atoms also open the graphite layer by pulling the carbon atoms at the interface. To illustrate this, we simulate the system with a low concentration of Li atoms (Li/C ratio of 0.104) such that a cloud of Li atoms is present at only some graphite layers. Figure 8(a) shows the density plot of Li atoms (blue) during an NVT simulation over a time period of 0.5 ns. To obtain the density plot, we first divided the simulation cell into a mesh of cubic boxes with dimensions ( $0.30 \text{ \AA} \times 0.30 \text{ \AA} \times 0.30 \text{ \AA}$ ). We then count the number of times a lithium atom was located in each of the grids through the entire length of the simulation and normalized these numbers by the highest count recorded in any of the grids. We used these values to obtain the resulting density plot in Figure 8. The blue color represents all grids (regions) that registered a Li count during the simulation. As shown in Figure 8(a), Li intercalates only into the layers near which a cloud of Li atoms was present. The intercalation stops when only a single row of Li atoms is present at the interface because of a lack of surrounding Li atoms that can push the Li into graphite.

The edge of the graphite anode for batteries is considered to be modified chemically, and oxidative terminations ( $-\text{H}$ ,  $-\text{OH}$ ,  $=\text{O}$ ,  $-\text{COOH}$ ) are one of the most common termination structures for graphite.<sup>44,45</sup> Experimental studies<sup>18,46</sup> observe that, in carbons that contain substantial amounts of hydrogen, the maximum amount of lithium that can be intercalated is proportional to the hydrogen content. We perform MD simulations of intercalation of Li through: (i) H-terminated armchair edges and (ii) two H-terminated zigzag edges of graphite to investigate the role of Li–H interactions in the intercalation of Li. The simulation settings are identical to the perfect edge case discussed above. We observe that the two H-terminated zigzag edges of graphite block the intercalation of Li as shown in Figure 8(c). In H-terminated graphite, Li

intercalates through the armchair edge as shown in Figure 8(d). We observe a similar intercalation mechanism where surrounding Li atoms assist in Li intercalation. However, in addition to the surrounding Li atoms, the H termination assists in a similar manner by pushing the Li atoms into graphite. We observe that, unlike in the perfect edge case, the intercalation does not stop when a single row of Li atoms is present at the interface; the H atoms at the interface are able to push the final row of Li into graphite. This agrees with the experimental observation<sup>18</sup> that the maximum amount of lithium that can be intercalated is proportional to the hydrogen content.

**E. Adsorption of Li Clusters on Top of Graphene, Defective Graphene, Reconstructed Graphene, and Graphite.** We investigated the formation energy of 1, 2, 3, and 4 Li atom clusters adsorbed over pristine graphene, graphene with single and divacancy, 5–8–5 reconstructed graphene, and 5–5–5–7–7–7 reconstructed graphene. The ReaxFF formation energies were obtained from energy minimization with a convergence criterion of 0.1 kcal/mol. The formation energies given by ReaxFF are in good agreement with our DFT results as shown in Figure 9.

We investigated Li adsorption on top of single and multilayer graphene using GCMC simulations. We observed that Li does not adsorb on defect-free single layer graphene (SLG), which makes it unsuitable for anode applications. This is in agreement with DFT studies,<sup>12,31</sup> which report positive adsorption energies for Li over graphene for Li content ranging from  $\text{Li}_{0.1}\text{C}_6$  to  $\text{Li}_6\text{C}_6$ . We observe the formation of metallic Li clusters over graphene at concentrations as low as  $x = 0.25$  in  $\text{Li}_x\text{C}_6$  with 4 Li atoms forming a prismatic cluster as shown in Figure 10. At higher concentrations, Li forms a metallic layer over single and multilayer graphene and does not exhibit the in-plane checkerboard ordering seen in graphite (see Figure 3a).

**F. Li Intercalation in Onion-Like Carbon Nanostructures (OLCs).** We investigated Li intercalation and diffusion in OLCs and explored their potential as an LIB anode material. Understanding Li diffusivity limitations in OLCs is imperative



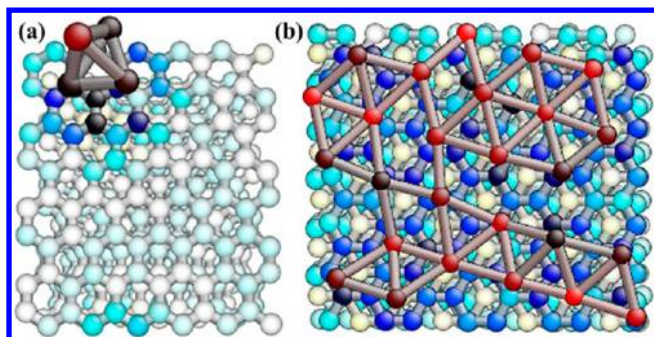


**Figure 10.** (a) Four Li atoms forming a prismatic cluster over 6-layer graphene. (b) Li atom forming a metallic layer over 6-layer graphene.

to optimizing them for charge/discharge rate performance. The OLCs were obtained from MD simulations by Ganesh et al.<sup>47</sup> We performed metadynamics simulations to obtain barriers for Li to diffuse out from an OLC. Intuitively, Li should diffuse from within the OLC to its exterior through defects. We consider an OLC with a diameter of 2 nm and explore the free energy surface of a Li adsorbed between a 12-membered ring in the outer layer and a 6-membered ring in the inner layer of the OLC using metadynamics simulations as implemented in the PLUMED package in LAMMPS.<sup>41</sup> The collective variable is the distance of the Li atom from the center of the 6-membered ring on which it is adsorbed, and the metadynamics simulation is run in the NVT ensemble at 600 K. A similar approach is used as in our earlier study to obtain the FES. Figure 11(a) shows the density plot of Li during a metadynamics simulation at 600 K, and the free energy landscape of Li diffusing out from the OLC is shown in Figure 11(b). The  $x$  axis is the distance of Li from the center of mass of the 6-membered ring within the OLC on which it is adsorbed and has an initial value of 2.15 Å. Even though the free energy minimum of Li is within the OLC, Li has a high energy barrier of  $\sim 24.8$  kcal/mol to diffuse into the OLC. The high barrier for Li diffusion into the OLC suggests that the OLC interior does not offer any accessible storage capacity for Li.

We perform molecular dynamics simulations with Li placed manually within the OLC as well as on its outer surface to investigate Li migration patterns. Figure 12 shows the density plot of Li (green) atoms in the simulation box during an NVT simulation at 1000 K obtained as an average over a time period of 250 ps. As discussed earlier, the green color represents all

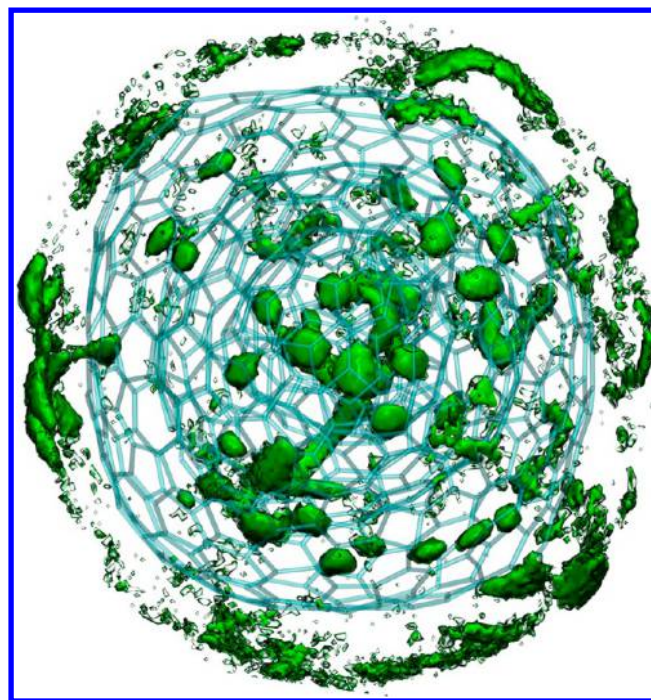


**Figure 12.** Density plot of Li (green) in an OLC during an NVT simulation at 1000 K.

grids (regions) that registered a Li count during the simulation. Because of the high barriers for Li diffusion between the layers of OLCs, we need high temperatures to observe Li diffusion between the OLC layers. We can see that Li outside the OLC has a higher diffusion constant than Li within the OLC and migrates freely on the outer surface of the OLC. However, most of the Li within the OLC is confined near its initial position, and a few diffuse between the OLC layers. This reiterates the observation from metadynamics simulations that, because of high diffusion barriers, the interior of OLC is inaccessible for energy applications and implies lower Li storage capacities in carbon onions. However, the outer surface of OLC offers sites for fast Li adsorption/desorption and is suitable for applications as electrode materials in supercapacitors, as was also demonstrated experimentally.<sup>48</sup>

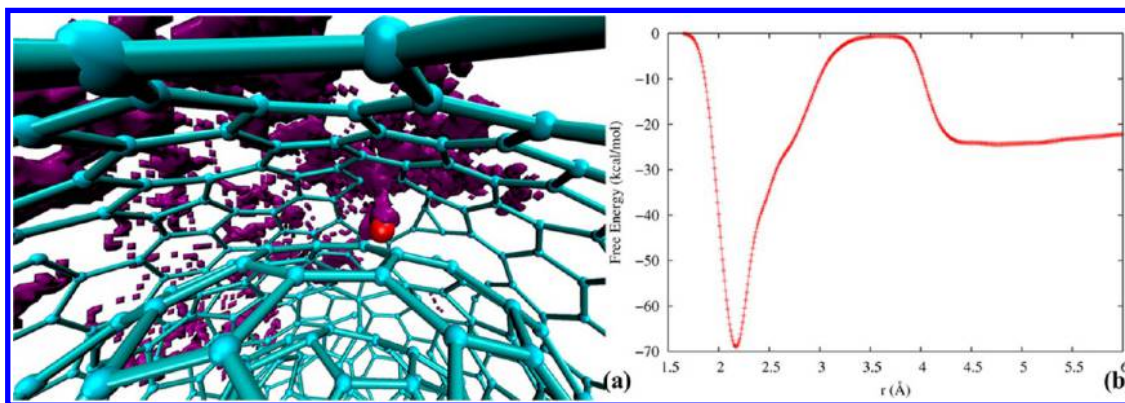


**Figure 11.** (a) Density plot of Li (purple) during a metadynamics simulation at 600 K. (b) Free energy landscape for Li diffusing out from the OLC through a 12-membered ring.

## IV. CONCLUSIONS

To conclude, we have developed and applied a ReaxFF reactive force field to describe Li/C interactions in carbon-based materials with and without defects. The Li/C ReaxFF reactive force field is able to describe energetics of Li adsorption as well as Li migration barriers in pristine/defective graphene and graphite. Molecular dynamics simulations suggest that a critical Li density is required to enable Li intercalation into graphite. The force field successfully obtains the stepped voltage profile of Li intercalation in graphite seen in experiments.<sup>38</sup> In the presence of vacancy defects, we observe an increase in the Li/C ratio and an upward shift in the voltage profile with both proportional to the number of vacancy defects. The larger adsorption energy of Li in defects explains the upward shift as well as the increase in the Li/C ratio in the presence of defects. The Li–Li separation in Li clusters adsorbed on divacancy defect sites approaches Li–Li separation in bcc Li metals and should initiate subsequent plating of Li metal at these sites as observed experimentally<sup>40</sup> in porous graphene networks. In carbon onions, we observe that the outer surface provides sites for Li adsorption with fast charging/discharging rates. However, the inner volume is inaccessible for Li intercalation due to high diffusion barriers.

We have successfully demonstrated that our force field enables investigation of energetics as well as kinetics of Li intercalation in carbon-based materials with and without defects using large-scale atomistic simulations, and that it can be a useful tool for atomistic understanding of novel processes in carbon nanostructures as well as in designing improved carbon (nano)materials for energy applications.

## AUTHOR INFORMATION

### Corresponding Authors

\*Adri C.T. van Duin, Associate Professor, Department of Mechanical and Nuclear Engineering, Pennsylvania State University, 136 Research East Building, University Park, PA 16802, USA. Phone: +1-814-863-6277. E-mail: acv13@psu.edu.

\*P. Ganesh, R & D Staff, Center for Nanophase Materials Sciences, Oak Ridge National Laboratory, Oak Ridge, TN 37831, USA. Phone: +1-865-574-1999. E-mail: ganeshp@ornl.gov.

### Notes

The authors declare no competing financial interest.

## ACKNOWLEDGMENTS

We acknowledge support from the Fluid Interface Reactions, Structures and Transport (FIRST) Center, an Energy Frontier Research Center funded by the U.S. Department of Energy, Office of Science, Office of Basic Energy Sciences. M.R. performed the ReaxFF fitting and calculations. A.C.T.v.D. and P.R.C.K. supervised the work and contributed to the design of the study. P.G. performed density functional calculations and significantly contributed to the design of the scope and writing of the paper at the Center for Nanophase Materials Sciences, which is sponsored at Oak Ridge National Laboratory by the Scientific User Facilities Division, Office of Basic Energy Sciences, U.S. Department of Energy. This research used resources of the National Energy Research Scientific Computing Center, a DOE Office of Science User Facility supported by the Office of Science of the U.S. Department of Energy under Contract No. DE-AC02-05CH11231.

## REFERENCES

- (1) Dresselhaus, M. S.; Dresselhaus, G. *Adv. Phys.* **2002**, *51*, 1–186.
- (2) Paulo, V. C. M.; Mota, F. d. B.; Artur, J. S. M.; Caio, M. C. d. C. *Nanotechnology* **2010**, *21*, 115701.
- (3) Yang, C.-K. *Appl. Phys. Lett.* **2009**, *94*, 163115.
- (4) Wang, X.; Zeng, Z.; Ahn, H.; Wang, G. *Appl. Phys. Lett.* **2009**, *95*, 183103.
- (5) Persson, K.; Hinuma, Y.; Meng, Y. S.; Van der Ven, A.; Ceder, G. *Phys. Rev. B* **2010**, *82*, 125416.
- (6) Persson, K.; Sethuraman, V. A.; Hardwick, L. J.; Hinuma, Y.; Meng, Y. S.; van der Ven, A.; Srinivasan, V.; Kostecki, R.; Ceder, G. *J. Phys. Chem. Lett.* **2010**, *1*, 1176–1180.
- (7) Guerard, D.; Herold, A. *Carbon* **1975**, *13*, 337–345.
- (8) Ohzuku, T.; Iwakoshi, Y.; Sawai, K. *J. Electrochem. Soc.* **1993**, *140*, 2490–2498.
- (9) Dahn, J. R. *Phys. Rev. B* **1991**, *44*, 9170–9177.
- (10) Zhao, X.; Hayner, C. M.; Kung, M. C.; Kung, H. H. *Adv. Energy Mater.* **2011**, *1*, 1079–1084.
- (11) Liu, M.; Kutana, A.; Liu, Y.; Yakobson, B. I. *J. Phys. Chem. Lett.* **2014**, *5*, 1225–1229.
- (12) Liu, Y.; Artyukhov, V. I.; Liu, M.; Harutyunyan, A. R.; Yakobson, B. I. *J. Phys. Chem. Lett.* **2013**, *4*, 1737–1742.
- (13) Xu, C.; Xu, B.; Gu, Y.; Xiong, Z.; Sun, J.; Zhao, X. S. *Energy Environ. Sci.* **2013**, *6*, 1388–1414.
- (14) Ganesh, P.; Kim, J.; Park, C.; Yoon, M.; Reboredo, F. A.; Kent, P. R. C. *J. Chem. Theory Comput.* **2014**, *10*, 5318–5323.
- (15) Xiao, S.; Zhu, H.; Wang, L.; Chen, L.; Liang, H. *Phys. Chem. Chem. Phys.* **2014**, *16*, 16003–16012.
- (16) Song, B.; Yang, J.; Zhao, J.; Fang, H. *Energy Environ. Sci.* **2011**, *4*, 1379–1384.
- (17) Meng, Y. S.; Arroyo-de Dompablo, M. E. *Energy Environ. Sci.* **2009**, *2*, 589–609.
- (18) Dahn, J. R.; Zheng, T.; Liu, Y.; Xue, J. S. *Science* **1995**, *270*, 590–593.
- (19) van Duin, A. C. T.; Dasgupta, S.; Lorant, F.; Goddard, W. A. *J. Phys. Chem. A* **2001**, *105*, 9396–9409.
- (20) Chenoweth, K.; van Duin, A. C. T.; Goddard, W. A. *J. Phys. Chem. A* **2008**, *112*, 1040–1053.
- (21) Plimpton, S. J. *Comput. Phys.* **1995**, *117*, 1–19.
- (22) te Velde, G.; Bickelhaupt, F. M.; Baerends, E. J.; Fonseca Guerra, C.; van Gisbergen, S. J. A.; Snijders, J. G.; Ziegler, T. *J. Comput. Chem.* **2001**, *22*, 931–967.
- (23) Islam, M. M.; Ostadhossein, A.; Borodin, O.; Yeates, A. T.; Tipton, W. W.; Hennig, R. G.; Kumar, N.; van Duin, A. C. T. *Phys. Chem. Chem. Phys.* **2015**, *17*, 3383–3393.
- (24) Ostadhossein, A.; Cubuk, E. D.; Tritsarlis, G. A.; Kaxiras, E.; Zhang, S.; van Duin, A. C. T. *Phys. Chem. Chem. Phys.* **2015**, *17*, 3832–3840.
- (25) Fan, F.; Huang, S.; Yang, H.; Raju, M.; Datta, D.; Shenoy, V. B.; Duin, A. C. T. v.; Zhang, S.; Zhu, T. *Modell. Simul. Mater. Sci. Eng.* **2013**, *21*, 074002.
- (26) Yang, H.; Huang, X.; Liang, W.; van Duin, A. C. T.; Raju, M.; Zhang, S. *Chem. Phys. Lett.* **2013**, *563*, 58–62.
- (27) Huang, X.; Yang, H.; Liang, W.; Raju, M.; Terrones, M.; Crespi, V. H.; van Duin, A. C. T.; Zhang, S. *Appl. Phys. Lett.* **2013**, *103*, 153901.
- (28) Grimme, S. *J. Comput. Chem.* **2006**, *27*, 1787–1799.
- (29) Kresse, G.; Hafner, J. *Phys. Rev. B* **1993**, *47*, 558–561.
- (30) Kresse, G.; Hafner, J. *Phys. Rev. B* **1994**, *49*, 14251–14269.
- (31) Lee, E.; Persson, K. A. *Nano Lett.* **2012**, *12*, 4624–4628.
- (32) Frisch, M. J.; Trucks, G. W.; Schlegel, H. B.; Scuseria, G. E.; Robb, M. A.; Cheeseman, J. R.; Scalmani, G.; Barone, V.; Mennucci, B.; Petersson, G. A.; Nakatsuji, H.; Caricato, M.; Li, X.; Hratchian, H. P.; Izmaylov, A. F.; Bloino, J.; Zheng, G.; Sonnenberg, J. L.; Hada, M.; Ehara, M.; Toyota, K.; Fukuda, R.; Hasegawa, J.; Ishida, M.; Nakajima, T.; Honda, Y.; Kitao, O.; Nakai, H.; Vreven, T.; Montgomery, J. A., Jr.; Peralta, J. E.; Ogliaro, F.; Bearpark, M. J.; Heyd, J.; Brothers, E. N.; Kudin, K. N.; Staroverov, V. N.; Kobayashi, R.; Normand, J.; Raghavachari, K.; Rendell, A. P.; Burant, J. C.; Iyengar, S. S.

Tomasi, J.; Cossi, M.; Rega, N.; Millam, N. J.; Klene, M.; Knox, J. E.; Cross, J. B.; Bakken, V.; Adamo, C.; Jaramillo, J.; Gomperts, R.; Stratmann, R. E.; Yazyev, O.; Austin, A. J.; Cammi, R.; Pomelli, C.; Ochterski, J. W.; Martin, R. L.; Morokuma, K.; Zakrzewski, V. G.; Voth, G. A.; Salvador, P.; Dannenberg, J. J.; Dapprich, S.; Daniels, A. D.; Farkas, Ö.; Foresman, J. B.; Ortiz, J. V.; Cioslowski, J.; Fox, D. J. *Gaussian 09*; Gaussian, Inc.: Wallingford, CT, 2009.

(33) Fan, X.; Zheng, W. T.; Kuo, J.-L. *ACS Appl. Mater. Interfaces* **2012**, *4*, 2432–2438.

(34) Senftle, T. P.; Meyer, R. J.; Janik, M. J.; van Duin, A. C. T. *J. Chem. Phys.* **2013**, *139*, 044109.

(35) Senftle, T. P.; van Duin, A. C. T.; Janik, M. J. *Catal. Commun.* **2014**, *52*, 72–77.

(36) Aydinol, M. K.; Kohan, A. F.; Ceder, G. J. *Power Sources* **1997**, *68*, 664–668.

(37) Datta, D.; Li, J.; Koratkar, N.; Shenoy, V. B. *Carbon* **2014**, *80*, 305–310.

(38) Takami, N.; Satoh, A.; Hara, M.; Ohsaki, T. *J. Electrochem. Soc.* **1995**, *142*, 371–379.

(39) Imai, Y.; Watanabe, A. *J. Alloys Compd.* **2007**, *439*, 258–267.

(40) Mukherjee, R.; Thomas, A. V.; Datta, D.; Singh, E.; Li, J.; Eksik, O.; Shenoy, V. B.; Koratkar, N. *Nat. Commun.* **2014**, *5*, 3710/1–10.

(41) Bonomi, M.; Branduardi, D.; Bussi, G.; Camilloni, C.; Provasi, D.; Raiteri, P.; Donadio, D.; Marinelli, F.; Pietrucci, F.; Broglia, R. A.; Parrinello, M. *Comput. Phys. Commun.* **2009**, *180*, 1961–1972.

(42) Nadler, M. R.; Kempier, C. P. *Anal. Chem.* **1959**, *31*, 2109–2109.

(43) Ganesh, P.; Kent, P. R. C.; Jiang, D.-e. *J. Phys. Chem. C* **2012**, *116*, 24476–24481.

(44) Figueiredo, J. L.; Pereira, M. F. R.; Freitas, M. M. A.; Órfão, J. J. M. *Carbon* **1999**, *37*, 1379–1389.

(45) Takazumi, K. *Jpn. J. Appl. Phys.* **2013**, *52*, 04CN08.

(46) Sato, K.; Noguchi, M.; Demachi, A.; Oki, N.; Endo, M. *Science* **1994**, *264*, 556–558.

(47) Ganesh, P.; Kent, P. R. C.; Mochalin, V. J. *Appl. Phys.* **2011**, *110*, 073506.

(48) Pech, D.; Brunet, M.; Durou, H.; Huang, P.; Mochalin, V.; Gogotsi, Y.; Taberna, P.-L.; Simon, P. *Nat. Nanotechnol.* **2010**, *5*, 651–654.